Green Chemistry

PAPER

View Article Online
View Journal | View Issue

Check for updates

Cite this: *Green Chem.*, 2020, **22**, 4975

Facile synthesis of B/g-C_3N_4 composite materials for the continuous-flow selective photo-production of acetone†

Uriel Caudillo-Flores,[a] Daily Rodríguez-Padrón,[b] Mario J. Muñoz-Batista,*[c] Anna Kubacka,[a] Rafael Luque[b,d] and Marcos Fernández-García*[a]

Received 15th April 2020,
Accepted 24th June 2020

DOI: 10.1039/d0gc01326a

rsc.li/greenchem

In this work versatile boron–carbon nitride composite materials were synthesized and utilized in a sustainable process using sunlight as the energy source for the continuous-flow selective photocatalytic production of acetone from 2-propanol. It is worth highlighting that the sample preparation was carried out by an environmentally friendly strategy, without a solvent or additional reagents. Samples containing boron in 1–10 wt% were subjected to physico-chemical characterization using XRD, porosimetry, UV-visible spectroscopy, TEM, energy-dispersive X-ray spectroscopy and XPS. The reaction output was analyzed on the basis of the reaction rate, selectivity and quantum efficiency of the process. A correlation analysis between catalytic properties with two observables, the boron phase distribution in the materials and charge handling efficiency (measured using photoluminescence), rationalizes photoactivity. Such an analysis indicates that the presence of an amorphous boron metallic phase and its contact with the carbon nitride component are key to setting up a renewable and easily scalable chemical process to obtain acetone.

Open Access Article. Published on 25 June 2020. Downloaded on 12/9/2025 12:21:23 PM.
This article is licensed under a Creative Commons Attribution-NonCommercial 3.0 Unported Licence.

Introduction

The exponential growth of human population and industrial activities urges chemistry to diversify the sourcing of raw materials and to decrease its impact on the environment by reducing or eliminating waste. Catalysis plays a key role in the chemical industry as it is present in at least one step of *ca.* 80% of the industrial chemical processes.[1] Catalytic processes are well established and continuously but slowly being optimized to decrease energy demand and increase activity, selectivity, stability and lifetime.[2] However, to accomplish the above goals, a deep revolution in catalysis, focusing on sustainability and circular use of materials in industrial processes, is required.[3] In this context, a particularly important effort in catalysis combines the use of renewable energy sources with catalysts obtained by facile and environmentally viable synthetic methods that drive the desired reaction from both activity and selectivity points of view, thus leading to highly efficient and sustainable chemical processes.

The most desired renewable energy source for any catalytic process is sunlight irradiation, which is a cost-free and endless (at least at the human scale) source. Catalytic materials that can use sunlight need to efficiently use the UV and visible electromagnetic ranges of the solar spectrum.[4,5] In addition, photocatalysts based on cheap and copiously available materials, such as carbon nitride, are required.[6] Graphitic carbon nitride (g-C_3N_4) consists of a graphite-like structure of tris-*z*-triazine layers connected through amino groups. As discussed in the literature, carbon nitride has good electronic and chemical properties and thermal stability. These properties have triggered the use of the g-C_3N_4 material in metal-free catalysis for many photochemical reactions such as organic photodegradation, water splitting or alcohol reforming.[7–11] Moreover, its use as the main component in composite catalysts to obtain sunlight-operated materials is a recent and hot topic presently explored in the current literature.[11–18]

Herein, we propose the use of composite materials containing boron and carbon nitride as a sunlight-operated catalytic system, utilized in a continuous flow process for selective photo-oxidation of alcohols to ketones. Metallic boron and doped boron have been used previously in titania-based

[a]*Instituto de Catálisis y Petroleoquímica, CSIC, C/Marie Curie 2, 28049-Madrid, Spain. E-mail: mfg@icp.csic.es*
[b]*Departamento de Quimica Organica, Universidad de Cordoba, Edificio Marie-Curie (C-3), Ctra Nnal IV-A, Km 396, Cordoba, Spain*
[c]*Department of Chemical Engineering, University of Granada, Av. de la Fuente Nueva S/N, 18071-Granada, Spain. E-mail: mariomunoz@ugr.es*
[d]*Peoples Friendship University of Russia (RUDN University), 6 Miklukho-Maklaya str., Moscow, 117198, Russia*

†Electronic supplementary information (ESI) available. See DOI: 10.1039/d0gc01326a

Open Access Article. Published on 25 June 2020. Downloaded on 12/9/2025 12:21:23 PM.
This article is licensed under a Creative Commons Attribution-NonCommercial 3.0 Unported Licence.

materials for photocatalytic applications.[19–26] In these processes, the use of boron improved the performance of the titania reference materials. In spite of the mentioned successful examples of the use of metallic boron as a modifier or co-catalyst in most common photocatalytic semiconductors, its combination with carbon nitride, to the best of our knowledge, has not been explored in the literature. Therefore, herein we present the synthesis of such boron–carbon nitride composite materials in a series of samples containing boron in quantities ranging from 1 wt% to 10 wt%. These materials have been tested in the gas-phase continuous-flow selective transformation of 2-propanol to acetone. The use of sunlight and the detailed analysis of UV and visible contributions have also been considered. In this way, outstanding yields can be achieved under all illumination (but particularly sunlight) conditions in the 2-propanol to acetone transformation using an easily synthesized combination of boron and carbon nitride components, thus leading to a truly renewable process.

Experimental

Materials

Following a previously described procedure, graphitic carbon nitride (g-C_3N_4), employed here as a support, was prepared by calcination of melamine, for 4 h, at 580 °C in a semi-closed system. The thermal treatment was carried out employing a heating rate of 5 °C min^{-1}.[14,18] Subsequently, catalyst preparation was performed following a mechanochemical approach (Scheme 1), using a Retsch PM100 planetary ball mill, with a 125 mL reaction chamber and eighteen 10 mm stainless steel balls. Appropriate amounts of the previously synthesized g-C_3N_4 and commercial boron (Sigma-Aldrich) were milled at 350 rpm for 15 min in order to obtain a series of 4 samples with different boron contents, ranging from 1 wt% to 10 wt%.

Characterization

XRD patterns were acquired using a Bruker D8 Advance Diffractometer with a LynxEye detector. The experiments were recorded in a 2θ scan range from 10° to 70°. Phase identification was carried out using the Bruker Diffrac-plus Eva software, supported by the Power Diffraction File database. Specific surface area, average pore volume and size were obtained with a Micromeritics equipment (model, ASAP 2010) following nitrogen adsorption at 77 K and using the Brunauer–Emmett–Teller (BET) method. Samples were degassed under flowing argon at 473 K for 2 h before nitrogen adsorption. Photoluminescence spectra were measured at room temperature on a photoluminescence spectrophotometer (PerkinElmer LS50B). The optical properties of the materials (transmission or diffuse reflection) were measured with a Shimadzu apparatus (model, UV2100) using $BaSO_4$ or Teflon as a reference for diffuse experiments. SEM-EDX micrographs were acquired using a JEOL-SEM JSM-7800 LV scanning microscope. Transmission electron microscopy images were obtained using a JEOL 2100F TEM/STEM microscope. XPS measurements were accomplished using an ultrahigh vacuum multipurpose surface analysis instrument Specs™. The samples were evacuated overnight under vacuum (10^{-6} Torr) and subsequently, measurements were performed at room temperature using a conventional X-ray source with a Phoibos 150-MCD energy detector. XPS CASA software was used for the analysis of the XPS results.

Catalytic experiments and quantum efficiency calculation

Photocatalytic activity and selectivity of the different *x*B/g-C_3N_4 powders were evaluated by the photodegradation of 2-propanol (Aldrich, 99%) in the gas phase. The photodegradation reactions were carried out in a continuous-flow annular photoreactor using a setup described elsewhere.[27] The catalyst amount employed for the photodegradation was 40 mg. The powder was suspended in 1 mL of ethanol, which was deposited on a Pyrex tube (cut-off at *ca.* 290 nm), and dried at room temperature to form a thin film. The gaseous mixture (prepared before entering the reaction system) in the reactor (100 mL min^{-1}) was obtained by mixing 2-propanol (Aldrich, 99.00%) with the N_2 flow, humidified at 90%. After flowing the mixture for 4–6 h in the dark (control test), the photocatalytic

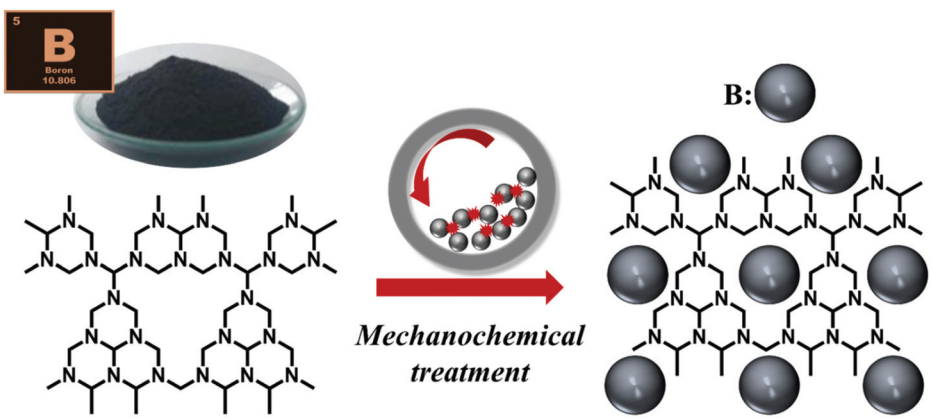

Scheme 1 Illustrative representation of the synthetic protocol.

 This journal is © The Royal Society of Chemistry 2020

Open Access Article. Published on 25 June 2020. Downloaded on 12/9/2025 12:21:23 PM.
This article is licensed under a Creative Commons Attribution-NonCommercial 3.0 Unported Licence.

experiments were carried out under UV-A (Philips TL 6 W/08-F6T5 BLB, 6 W) or sunlight-type (Philips TL54-765, 6 W) irradiation. For visible light experiments, we used sunlight-type lamps and a flexible polyester filter made from a deeply dyed PET material to absorb ultraviolet rays. In all cases, four fluorescent lamps symmetrically positioned outside the photoreactor were used (see the configuration in ESI, Fig. S1†). Reaction rates were evaluated under steady-state conditions, typically achieved after *ca.* 2 h from the start of irradiation. Stability of the catalytic properties was tested for 24 h. The concentration of the reactants and the products was analyzed using an online gas chromatograph (Agilent GC 6890) equipped with HP-PLOT-Q/HP-Innowax columns (0.5/0.32 mm I.D. × 30 m) and TCD/FID detectors. The carbon balance was calculated in all reaction experiments, and values above 98% were obtained. Selectivity data are presented as percentages on a molar carbon basis.

According to the IUPAC recommendation, the quantum efficiency was calculated as the ratio of the number of molecules reacting to the number of photons interacting with the sample (eqn (1)).[28]

$$\text{Q.E.}(\%) = 100 \times \frac{\langle r \rangle (\text{mol m}^{-2}\,\text{s}^{-1})}{\langle e^{a,s} \rangle (\text{Einstein m}^{-2}\,\text{s}^{-1})} \quad (1)$$

where r is the reaction rate normalized by the catalytic area and $\langle e^{a,s} \rangle$ is the averaged local superficial rate of photon absorption (also described in the literature as LSRPA).[29,30] The first observable is defined in eqn (2), and the $\langle e^{a,s} \rangle$ observable is defined by eqn (3).[30,31]

$$\langle r \rangle = Q\left(\frac{\langle C_0 \rangle - \langle C \rangle}{m\, S_A}\right) \quad (2)$$

$$e^{a,s}\ (x) = q_{sup}\ (x)\ F_{As} \quad (3)$$

In eqn (2), C and C_0 are the concentrations of the target organic molecule at times t and $t = 0$, Q is the total flow, S_A is the BET area ($m^2\ g^{-1}$) and m is the mass used in the reaction. In eqn (3), F_{As} is the fraction of light absorbed by the sample and q_{sup} is the radiation flux at each position ($\underline{x} = x, y, z$) of the catalytic film. The surface average of the $e^{a,s}$ observable is used in eqn (1). The q_{sup} term and calculation are described in ref. 27.

Results and discussion

Catalyst characterization

Through this work, a simple solvent-free mechanochemical procedure was developed for the preparation of boron-modified g-C_3N_4. It is worth noting that the use of mechanochemistry leads to a strong sustainable character since it allows the preparation of outstanding materials in short reaction times (in this case 15 min) and, additionally, avoids the use of solvents and/or other reagents, which are otherwise required by conventional methods.

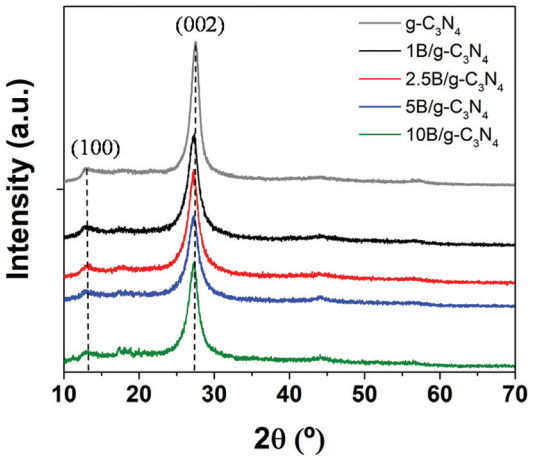

Fig. 1 XRD patterns of the prepared materials.

The prepared materials have been fully characterized utilizing a multi-technique strategy. In particular, the crystal structure and arrangement of the samples were investigated by XRD analysis (Fig. 1). XRD patterns of the five studied samples showed the presence of two main crystallographic peaks located at 13.1° and 27.4°, which are attributed to the (100) and (002) planes of typical g-C_3N_4-based materials.[7,14] Even if a certain decrease of intensity was observed for the obtained diffractograms after the incorporation of boron, no considerable changes on the main structure of the carbon nitride phase were found. Hence, these results validated the suitability of mechanochemical procedures for the modification of g-C_3N_4, without affecting its structure by controlling the milling conditions. Moreover, no clear evidence of boron incorporation was found by XRD analysis, although the mild decrease in crystallinity may be associated with it.[32,33] Such a result is further discussed in the following paragraphs.

The textural properties of the studied materials were analyzed by N_2-physisorption analysis (Table 1). The g-C_3N_4 sample showed surface area, pore volume and pore size within the range of the expected and reported values for this kind of material, in accordance with other reports in the literature.[14,34,35] Additionally, boron incorporation led to a loss of 50% of the initial surface area, which was not further affected by the different boron concentrations. Such results suggested that the observed changes in the textural properties

Table 1 Textural and optical features of the synthesized samples

Catalyst	BET surface area ($m^2\ g^{-1}$)	Pore volume ($m^3\ g^{-1}$)	Pore size (nm)	Band gap (eV)
g-C_3N_4	17.8	0.101	16.1	2.7
g-C_3N_4 (M)[a]	13.0	0.046	17.6	2.7
1B/g-C_3N_4	11.6	0.047	19.7	2.68
2.5B/g-C_3N_4	10.5	0.047	21.6	2.67
5B/g-C_3N_4	10.3	0.042	17.5	2.62
10B/g-C_3N_4	10.4	0.038	16.5	2.53

[a] The pristine g-C_3N_4 sample was mechanochemically treated.

Open Access Article. Published on 25 June 2020. Downloaded on 12/9/2025 12:21:23 PM.
This article is licensed under a Creative Commons Attribution-NonCommercial 3.0 Unported Licence.

were associated not exclusively (or at least not completely) with the direct functionalization with boron, but instead with the disruption of the g-C_3N_4 structure induced by the employed mechanochemical strategy. Accordingly, pore volume values exhibited a similar tendency, while pore sizes remained stable between 16.0 and 22.0 nm. Therefore, it is important to highlight that neither the process of mechanochemistry nor the increment of the boron content affects considerably the textural properties of the samples. This behavior could be beneficial for the catalytic behavior, allowing the incorporation of more active species without affecting the surface area of the final structures.

The laminar structure of the carbon nitride component is observed in the TEM micrographs shown in Fig. 2 (panels A and B). As is well known, this laminar structure is mainly responsible for the morphological properties presented in Table 1. The presence of boron in the composite materials is easily identified as part of the darkest zones in the low-magnification images shown in Fig. 2 (panels C and E). More detailed views obtained at higher magnifications (Fig. 2D and F) show isolated particles of boron in the *ca.* 5–20 nm range for all the studied samples. In addition, certain modifications of the support around the boron particles for the 10B/g-C_3N_4 sample were observed. Amorphization of the boron-neighboring zones of carbon nitride apparently takes place in accordance with the change of textural properties presented in Table 1. The amorphization corresponds to dark zones that are visible in the high-resolution micrographs presented in Fig. 2.

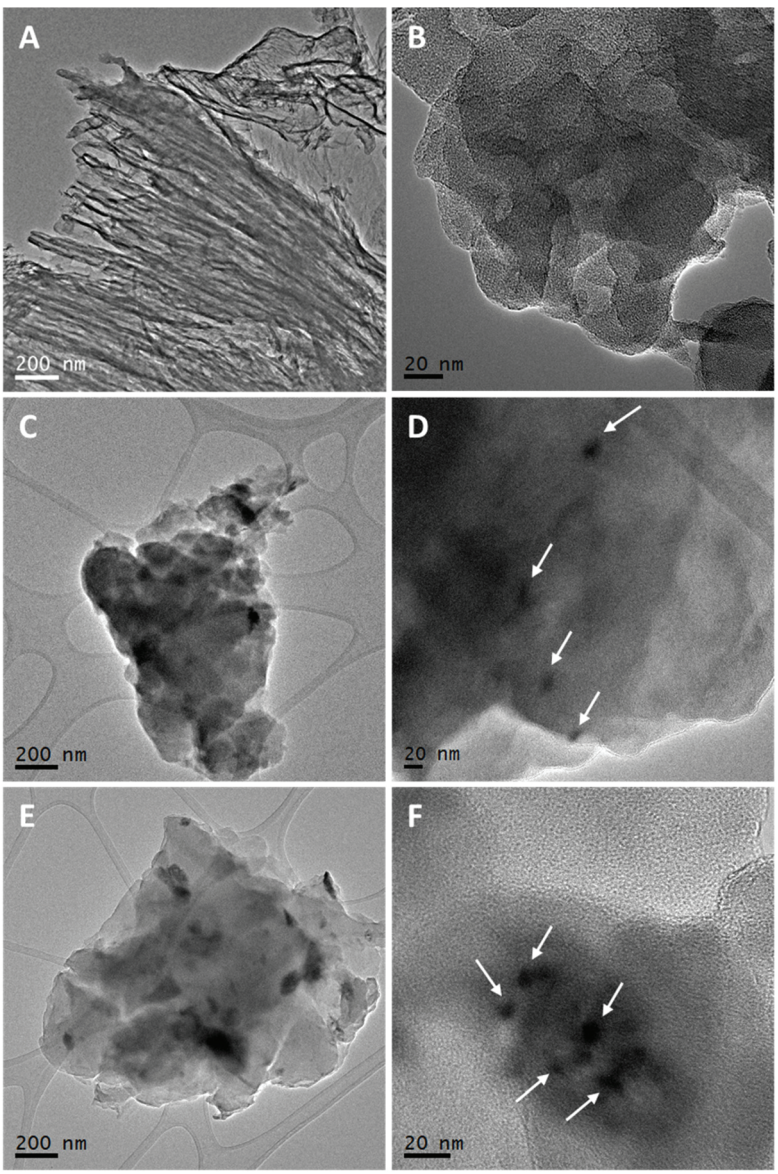

Fig. 2 TEM and HRTEM images of the g-C_3N_4 (A, B), 2.5B/g-C_3N_4 (C, D) and 10B/g-C_3N_4 (E, F) samples. Arrows indicate the position of boron particles.

This journal is © The Royal Society of Chemistry 2020

Open Access Article. Published on 25 June 2020. Downloaded on 12/9/2025 12:21:23 PM.
This article is licensed under a Creative Commons Attribution-NonCommercial 3.0 Unported Licence.

A potential inclusion of B in the carbon nitride structure may concomitantly occur for samples with the B content above 2.5 wt%.

To clarify the chemical composition of the carbon nitride zones adjacent to B nanoparticles and the evolution of the zones in relation with the total B content of the materials, a TEM–EDX analysis of selected samples is presented in Fig. S2.† The quantitative analysis in terms of the B/C + N ratio shows that the darkest zones in the 10B/g-C_3N_4 sample display two distinctive zones of B content, zones likely corresponding to B nanoparticles (A3–A5) and zones where the presence of B is significantly lower (A2, A6, and A7). Both zones display a higher B content than other, more "clear" zones, separated from the boron nanoparticles. We note that the zone of an intermediate B content is not detected in the case of the 2.5B/g-C_3N_4 sample. Microscopy analysis (Fig. 2 and S2†) strongly suggests the existence of two B-rich zones. The first zone is associated with the presence of B nanoparticles, a fact shared by all the samples. For such zones the nanoparticles are present as separate nanoparticles as well as coalesced in agglomerates, presenting in a few cases a relatively high secondary particle size of dozens of nanometers (Fig. 2). The second zone may contain smaller B nanoparticles, but the high-resolution micrographs and EDS analyses (Fig. 2 and S2†), as well as the two distinctive B 1s XPS signals for loadings above 2.5 wt% (see below) strongly suggest that doping of the carbon nitride structure by B takes place and it is the dominant chemical species containing B in such zones.

The chemical properties of the designed materials were thus analyzed by XPS measurements. XPS spectra revealed the presence of carbon, nitrogen and boron in the catalysts. Fig. 3 provides an overview of the N 1s, C 1s and B 1s regions. As can be seen in Fig. 3, the spectra for both N 1s and C1 of the g-C_3N_4 reference present the typical shapes as well as the peak positions (398.6 and 288.1 eV for N 1s and C 1s, respectively) of previous reports.[13] The N 1s and C 1s regions show that B incorporation into the composite materials has a limited influence on the respective XPS spectra for the 1 wt% and 2.5 wt% loadings. At 5 wt% loading, there are visible changes but only in the C 1s XPS spectra, while at the highest loading (10 wt%), both C 1s and N 1s XPS profiles display significant changes. Concomitant changes are observed in the B 1s region. At low loadings, we can observe a dominant contribution at 186.7 eV, characteristic of metallic boron.[36] For the 10 wt% loading (and a rather weak shoulder for the 5 wt% loading), an additional contribution at *ca.* 191.7 eV is observed. This contribution is between the boron oxides and hydroxides (above 193.0 V) and the hexagonal boron nitride (190.0 eV), and can be assigned to the interaction of B and N atoms (B in threefold coordination with N atoms), indicating that some of the boron atoms are introduced into the g-C_3N_4 structure. B replaces C atoms in the carbon nitride network.[37]

A detailed analysis of the boron effect on the C 1s and N 1s XPS peaks was carried out. A summary of the fitting results is presented in Fig. 4 for the representative samples. As previously mentioned, the pure g-C_3N_4 reference and the composite samples with loadings from 1 wt% to 5 wt% present similar N 1s XPS spectra with three main contributions, related to C_3–N (N_{3c}), N–C=N (N_{2c}), and N–H_x contributions. This result is shown in Fig. 4A for the 1B/g-C_3N_4 sample. Peaks at the C 1s XPS region (Fig. 4C) showed three contributions assigned to C–C, N–C=N and C–NH_x (related with the N–H_x contribution mentioned earlier at the N 1s peak) bonds of the carbon nitride component. As is well known, the intensity of the carbon–carbon contribution also arises from spurious carbonaceous entities (C–C/C=C). For the samples having 5 wt% and 10 wt% B loadings, additional contributions directly associated with the boron species present at the carbon nitride

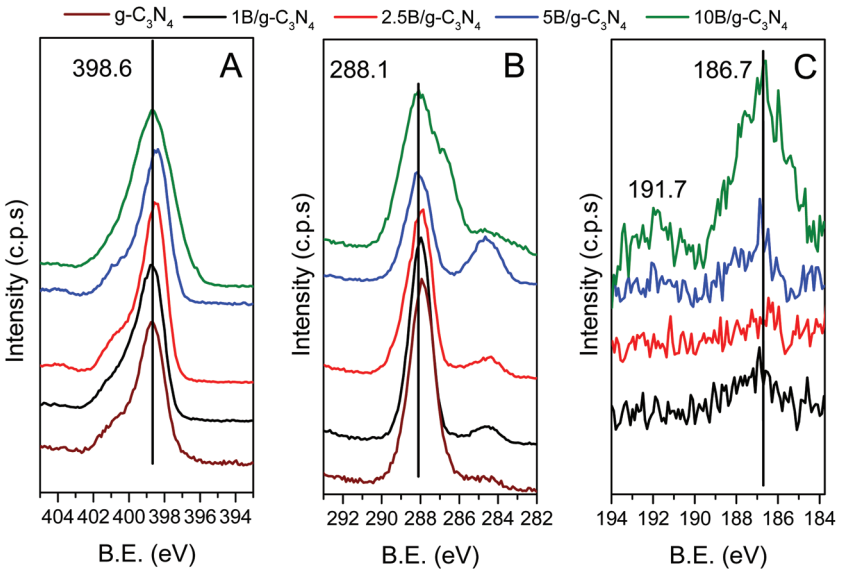

Fig. 3 XPS spectra of the prepared samples in the N 1s (A), C 1s (B) and B 1s (C) regions.

Open Access Article. Published on 25 June 2020. Downloaded on 12/9/2025 12:21:23 PM.
This article is licensed under a Creative Commons Attribution-NonCommercial 3.0 Unported Licence.

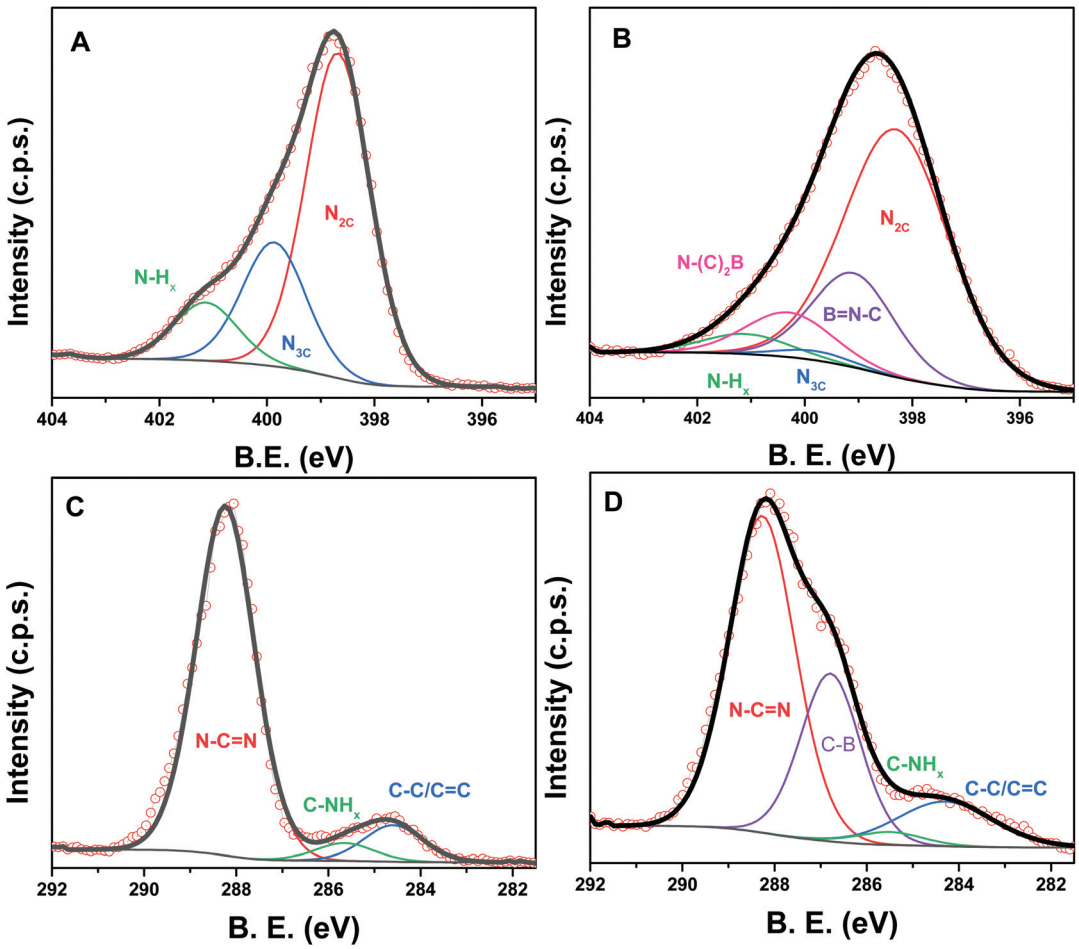

Fig. 4 Details of XPS fitting in the N 1s (A, B) and C 1s (C, D) regions for the 1B/g-C_3N_4 (A, C) and 10B/g-C_3N_4 (B, D) samples.

network are detected, as shown for the 10B/g-C_3N_4 sample in Fig. 4. In these cases, the N 1s and C 1s XPS regions displayed two (corresponding to B=N–C and N–(C_2)B bonds) and one (C–B bond) contributions, respectively.[14,15,38–40] The presence of these B-related signals justified the strong shape changes observed in the N 1s and C 1s XPS regions for the tested higher loading (Fig. 3).

From the detailed analysis of the XPS spectra (Fig. 3 and 4), we can thus provide evidence for the presence of a dominant metallic boron species, which according to XRD is essentially amorphous. In addition, in the 5 wt% loading of boron, XPS revealed the presence of a minor boron doping species at the carbon nitride network. According to the discussion of Fig. 3 and 4, this doping process takes place by substitution of carbon atoms by boron and leads to the appearance of C–B and C–N bonds in the carbon nitride structure. The analysis of the corresponding intensities at the B 1s XPS region indicates that this last (doping) species has a negligible presence for loadings below 2.5 wt%, while it is less than 10% of the total B content of the 5B/g-C_3N_4 sample and *ca.* 28% in the 10B/g-C_3N_4 sample.

The characterization of the samples is completed with the spectroscopic examination of their optical properties. The UV-visible spectra of the samples are shown in Fig. 5. The spectra are dominated by the carbon nitride component (the component dominating the molar content of the materials) and show a decay at the band gap region of the semiconductor

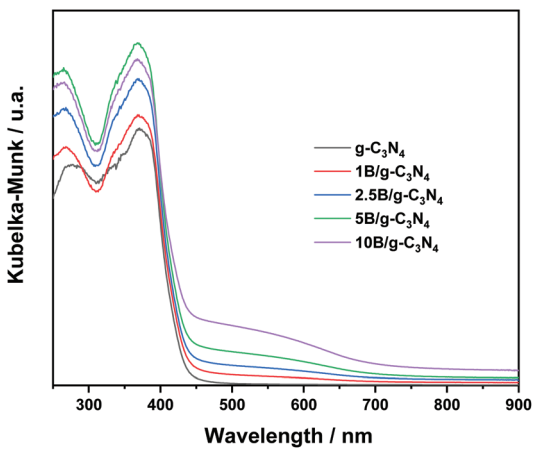

Fig. 5 UV-visible spectra of the samples.

This journal is © The Royal Society of Chemistry 2020

Open Access Article. Published on 25 June 2020. Downloaded on 12/9/2025 12:21:23 PM.
This article is licensed under a Creative Commons Attribution-NonCommercial 3.0 Unported Licence.

around 400–450 nm. Considering that graphitic carbon nitride is an indirect gap semiconductor, the calculated band gap energies are presented in Table 1.[7,9,41]

The band gap values are constant within an experimental error for the two lower loadings (1, 2.5 wt%) and then decrease by a maximum of *ca.* 0.2 eV for the rest of the samples. This behavior is clearly related to the presence of the doped boron species at the carbon nitride component for loadings equal to or above 5 wt%. In addition, the spectra showed a broad absorption bump below the region of the carbon nitride band gap. The intensity bump evolves gradually with the boron content and is thus ascribable to the amorphous boron component. This is in accordance with the existence of a semiconductor with a band gap of *ca.* 1.4 eV, as described in previous reports.[42]

In summary, mechanochemical synthesis generates a composite material consisting of amorphous metallic boron and carbon nitride components for boron loadings below or equal to 2.5 wt%. This leads to contact between two semiconductors with very different band gap energies, potentially allowing a large profit of the UV and visible components of the sunlight light. Their contact can be analyzed considering the conduction and valence band positions of the semiconductors, which provides evidence that an efficient charge separation takes place under illumination.[43] For around 2.5 wt% boron loading, we observe several physico-chemical phenomena, the insertion of boron into the carbon nitride component and a significant loss of crystallinity in the local environment of this doping process.

Catalytic performance and interpretation

The catalytic results corresponding to the photo-oxidation of 2-propanol are shown in Fig. 6. This figure shows measurements of the catalytic performance of the samples using the reaction rate and quantum efficiency observables obtained under UV and sunlight illumination conditions. All composite samples increase the activity of the reference systems (the boron reference has negligible activity, an order of magnitude below the carbon nitride). Using the most accurate analysis of activity and thus the quantum efficiency values, we can see that boron increases the activity of the carbon nitride reference by a maximum factor of 2.2 (UV) and 3.0 (sunlight). Both the maximum enhancement factors take place for the 2.5B/g-C_3N_4 sample. Interestingly, the control experiment carried out using pristine g-C_3N_4 after the milling process using the same conditions of synthesis as for g-C_3N_4–M confirmed that the mechanochemical synthetic conditions do not affect significantly the activity of the bare support (Fig. 6). Nevertheless, the mechanochemical process would provide a suitable interaction between B and the g-C_3N_4 components in composite samples, a fact that is shown in Fig. 6, but does not occur in a simple physical mixture (2.5B/g-C_3N_4-PM).

It is worth highlighting that the activity increase is maximized under sunlight illumination. A clear analysis of the measured enhancement factors allows us to conclude that the 2.5B/g-C_3N_4 composite benefits from both UV and visible illumination ranges but particularly from the latter (see Fig. S3†). Thus, it could be clearly stated that our system is an optimum choice for the efficient use of sunlight.

As shown in Fig. 7, carbon nitride provides a reasonably high selectivity to the partial oxidation compound, acetone, with a limited quantity (*ca.* 15%) of the second product, CO_2, corresponding to the total oxidation of the reactant. This selectivity to partial oxidation increases significantly for the composite sample displaying maximum activity, *i.e.* for the 2.5B/g-C_3N_4 catalyst. This sample has a selectivity to acetone approaching 98.5%, which is higher than those for all the previously reported materials, including titania-based materials.[15,44–52] Together with the outstanding activity presented by the composite samples, these results indicated that the B/g-C_3N_4 composite is a highly active and selective material.

To interpret catalytic activity, we first analyzed the photoluminescence of the samples under UV (320 nm) and visible

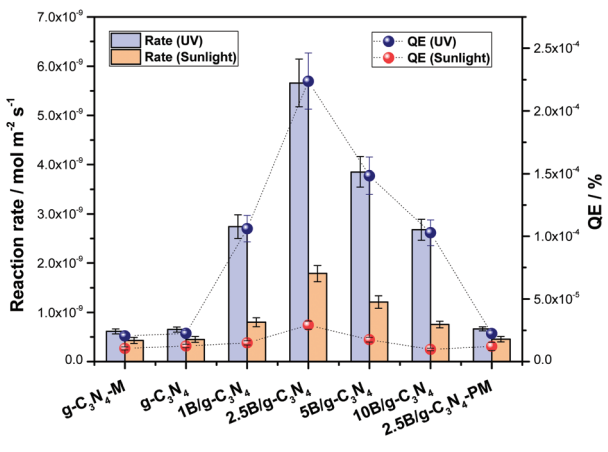

Fig. 6 Reaction rate and quantum efficiency of the 2-propanol photo-oxidation for the samples under UV and sunlight-type illumination.

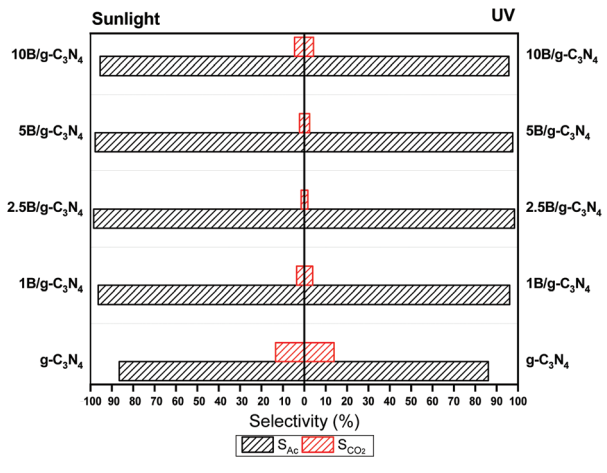

Fig. 7 Selectivity of the 2-propanol photo-oxidation for the samples under UV and sunlight-type illumination.

Open Access Article. Published on 25 June 2020. Downloaded on 12/9/2025 12:21:23 PM.
This article is licensed under a Creative Commons Attribution-NonCommercial 3.0 Unported Licence.

(425 nm) illumination conditions. Fig. 8 presents the results for the two excitation conditions. In both the conditions, the photoluminescence spectra of the composite samples are dominated by the major carbon nitride component with relatively minor changes among the composite samples with respect to spectral shape. The main differences are related to the intensity of the signal, which is known to be a measure of the charge recombination.[4,7] All B/g-C_3N_4 composite samples display decreasing intensity with respect to the carbon nitride reference for all the tested illumination conditions. The largest intensity decrease between two samples occurs between the carbon nitride reference and the 1B/g-C_3N_4 material. This clearly demonstrates that the abovementioned contact between the amorphous metallic boron and carbon nitride semiconductors has a profound effect on charge separation after illumination, irrespective of the wavelength (and thus related to the excitation of one of the components). This positive effect on charge separation takes place for all samples in accordance with the increasing contact between the two semiconductors. However, as shown in the correlation plots in Fig. 8, the existence of a second boron species, namely the species doping the carbon nitride structure, triggers a negative impact on catalytic activity. The shadow area in the panels of Fig. 8 indicates that the negative impact on the activity is directly proportional to the amount of boron doping of the carbon nitride for all illumination conditions (see the trend occurring from the 2.5B/g-C_3N_4 sample, having maximum activity, to samples having higher loadings). Only the samples free of this doping boron species (and then displaying 100% of metal B in Fig. 8) are free of the negative effects on catalytic properties. Maximum activity is thus not only related to a larger contact between the amorphous boron and carbon nitride components but also to the negative effects related to the doping process of carbon nitride. The negative effect is likely related to the decrease of crystallinity in the neighbourhood of the boron doping (as suggested by TEM–EDX and XRD) and thus, is likely a consequence of the preparation procedure. Disturbing the carbon nitride crystallinity (in our case as a collateral effect of the B doping process detected by XPS and TEM–EDX) affects charge separation and effective mean free path,[9,53] decreasing the ability of the charge carrier species to interact with chemical molecules. The 2.5B/g-C_3N_4 catalyst activity and outstanding selectivity properties are thus the optimum achieved through a balance between positive and negative effects taking place as the boron quantity increases in the composite samples.

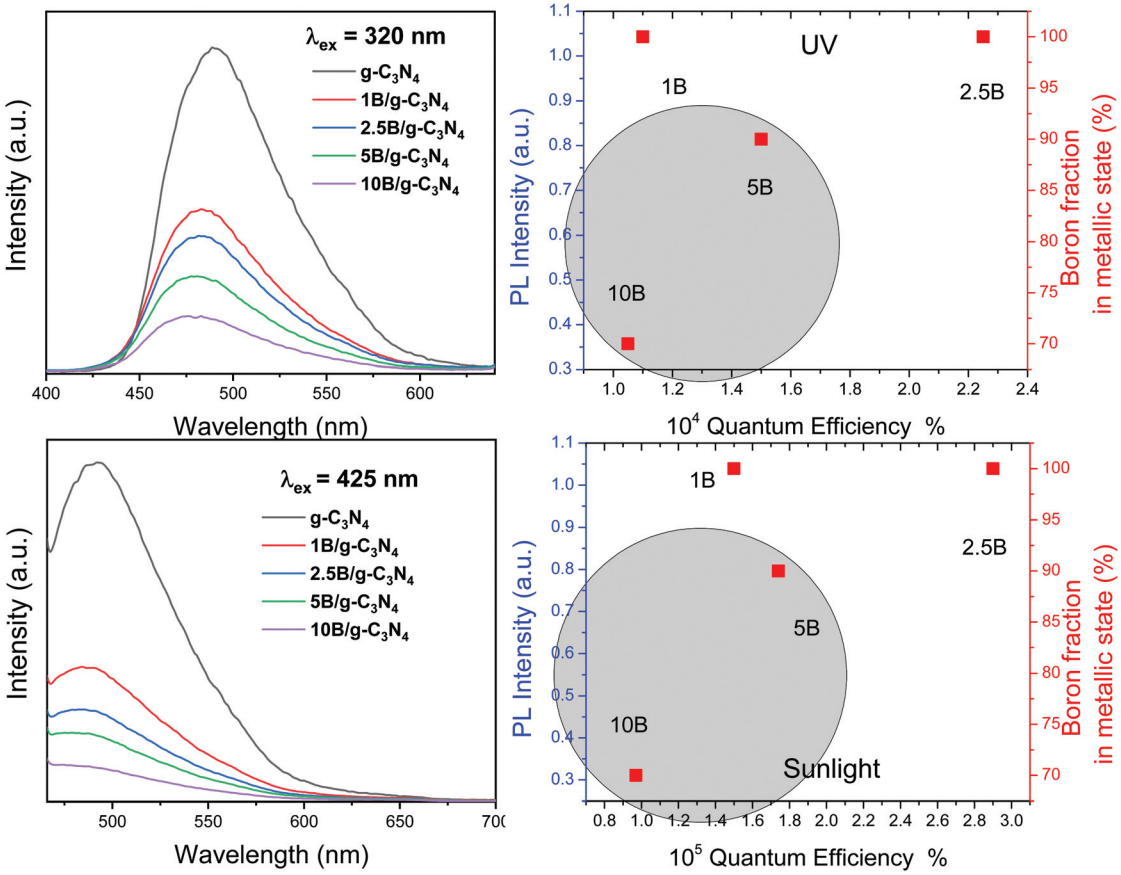

Fig. 8 Photoluminescence of the samples under UV (320 nm) and visible (425 nm) light excitation. Correlation plot between quantum efficiency and photoluminescence activity or boron metal percentage. Shadow zones highlight the region with the presence of boron in the carbon nitride network.

This journal is © The Royal Society of Chemistry 2020

Open Access Article. Published on 25 June 2020. Downloaded on 12/9/2025 12:21:23 PM.
This article is licensed under a Creative Commons Attribution-NonCommercial 3.0 Unported Licence.

Conclusions

B/g-C_3N_4 materials were synthesized using a facile and green mechanochemical protocol. Remarkably, the aforementioned methodology could trigger the sustainable development of cost-effective protocols for nanomaterial synthesis, avoiding excess reagents or the use of solvents, as well as decreasing reaction times, and hence energy consumption. Moreover, increasing the boron content in the system generates different types of materials. Up to 2.5 wt% loading, a binary system consisting of amorphous metallic boron nanoparticles supported on a carbon nitride compound was obtained. Above this point, the carbon nitride component is doped with boron. In such case, a minor part of boron (a maximum of *ca.* 30% in the 10B/g-C_3N_4 sample) occupies the carbon positions of the carbon nitride component network.

The composite system provides high activity and selectivity in the photo-oxidation of 2-propanol to acetone. The optimum activity is achieved with a 2.5B/g-C_3N_4 sample, which leads to outstanding activity and near-complete selectivity to the conversion of the alcohol moiety into the corresponding ketone. The above discovery unveils the potential of the B/g-C_3N_4 composite system (consisting of amorphous metallic nanoparticles supported on carbon nitride) for partial oxidation reactions under continuous-flow and sunlight illumination conditions. This leads to a candidate to scale up such type of partial oxidation reaction with a truly renewable process.

Conflicts of interest

There are no conflicts to declare.

Acknowledgements

Financial support from MINECO (Spain; ENE2016-77798-C4-1-R grant), CSIC and the Secretaria de Ciencia Tecnología e Innovacion of CDMX (SECTEI, Mexico) is gratefully acknowledged. M. Fernández-García acknowledges the fruitful general discussions with Prof. F. Fernández-Martín. M. J. Muñoz-Batista thanks the "Plan Propio de Investigación-Proyectos de investigación precompetitivos para Jóvenes Investigadores" from UGR. Rafael Luque gratefully acknowledges MINECO for funding the project CTQ2016-78289-P, co-financed with FEDER funds. Daily Rodriguez-Padron also gratefully acknowledges MINECO for providing a research contract under the same project. The publication has been prepared with support from the RUDN University Program 5-100.

Notes and references

1 D. Rodríguez-Padrón, A. R. Puente-Santiago, A. M. Balu, M. J. Muñoz-Batista and R. Luque, *ChemCatChem*, 2019, **11**, 18–38.
2 J. A. Moulijn, M. Makkee and A. E. van Diepen, *Chemical Process Technology*, John Wiley & Sons, 2nd edn, 2013.
3 P. Lanzafame, S. Perathoner, G. Centi, S. Gross and E. J. M. Hensen, *Catal. Sci. Technol.*, 2017, **7**, 5182–5194.
4 A. Kubacka, M. Fernández-García and G. Colón, *Chem. Rev.*, 2012, **112**, 1555–1614.
5 J. C. Colmenares and R. Luque, *Chem. Soc. Rev.*, 2014, **43**, 765–778.
6 D. Rodríguez-Padrón, R. Luque and M. J. Muñoz-Batista, *Top. Curr. Chem.*, 2020, **378**, 1–28.
7 W.-J. Ong, L.-L. Tan, Y. H. Ng, S.-T. Yong and S.-P. Chai, *Chem. Rev.*, 2016, **116**, 7159–7329.
8 C. Yanjuan, W. Yuxiong, W. Hao and C. Fangyan, *Prog. Chem.*, 2016, **28**, 428–437.
9 I. F. Teixeira, E. C. M. Barbosa, S. C. E. Tsang and P. H. C. Camargo, *Chem. Soc. Rev.*, 2018, **47**, 7783–7817.
10 K. H. Leong, P. F. Lim, L. C. Sim, V. Punia and S. Pichiah, *Appl. Surf. Sci.*, 2018, **430**, 355–361.
11 A. Akhundi, A. Badiei, G. M. Ziarani, A. Habibi-Yangjeh, M. J. Muñoz-Batista and R. Luque, *Mol. Catal.*, 2020, **488**, 110902.
12 B. Lin, H. An, X. Yan, T. Zhang, J. Wei and G. Yang, *Appl. Catal., B*, 2017, **210**, 173–183.
13 M. J. Muñoz-Batista, O. Fontelles-Carceller, M. Ferrer, M. Fernández-García and A. Kubacka, *Appl. Catal., B*, 2016, **183**, 86–95.
14 M. J. Muñoz-Batista, O. Fontelles-Carceller, A. Kubacka and M. Fernández-García, *Appl. Catal., B*, 2017, **203**, 663–672.
15 O. Fontelles-Carceller, M. J. Muñoz-Batista, M. Fernández-García and A. Kubacka, *ACS Appl. Mater. Interfaces*, 2016, **8**, 2617–2627.
16 I. Majeed, U. Manzoor, F. K. Kanodarwala, M. A. Nadeem, E. Hussain, H. Ali, A. Badshah, J. A. Stride and M. A. Nadeem, *Catal. Sci. Technol.*, 2018, **8**, 1183–1193.
17 N. F. F. Moreira, M. J. Sampaio, A. R. Ribeiro, C. G. Silva, J. L. Faria and A. M. T. Silva, *Appl. Catal., B*, 2019, **248**, 184–192.
18 M. J. Muñoz-Batista, D. Rodríguez-Padrón, A. R. Puente-Santiago, A. Kubacka, R. Luque and M. Fernández-García, *ChemPhotoChem*, 2018, **2**, 870–877.
19 L. Chen, X. Zhou, B. Jin, J. Luo, X. Xu, L. Zhang and Y. Hong, *Int. J. Hydrogen Energy*, 2016, **41**, 7292–7300.
20 M. L. Yola, T. Eren and N. Atar, *Chem. Eng. J.*, 2014, **250**, 288–294.
21 W. Zhang, T. Hu, B. Yang, P. Sun and H. He, *J. Adv. Oxid. Technol.*, 2013, **16**, 261–267.
22 A. Zaleska, J. W. Sobczak, E. Grabowska and J. Hupka, *Appl. Catal., B*, 2008, **78**, 92–100.
23 A. Zaleska, E. Grabowska, J. W. Sobczak, M. Gazda and J. Hupka, *Appl. Catal., B*, 2009, **89**, 469–475.
24 E. Grabowska, A. Zaleska, J. W. Sobczak, M. Gazda and J. Hupka, in *Procedia Chemistry*, Elsevier, 2009, vol. 1, pp. 1553–1559.
25 E. Bilgin Simsek, *Appl. Catal., B*, 2017, **200**, 309–322.
26 R. Khan, S. W. Kim, T. J. Kim and C. M. Nam, *Mater. Chem. Phys.*, 2008, **112**, 167–172.

Open Access Article. Published on 25 June 2020. Downloaded on 12/9/2025 12:21:23 PM.
This article is licensed under a Creative Commons Attribution-NonCommercial 3.0 Unported Licence.

27 M. J. Muñoz-Batista, A. Kubacka, A. B. Hungría and M. Fernández-García, *J. Catal.*, 2015, **330**, 154–166.
28 S. E. Braslavsky, A. M. Braun, A. E. Cassano, A. V. Emeline, M. I. Litter, L. Palmisano, V. N. Parmon and N. Serpone, *Pure Appl. Chem.*, 2011, **83**, 931–1014.
29 G. E. Imoberdorf, A. E. Cassano, O. M. Alfano and H. A. Irazoqui, *AIChE J.*, 2006, **52**, 1814–1823.
30 M. J. Muñoz-Batista, M. M. Ballari, A. Kubacka, O. M. Alfano and M. Fernández-García, *Chem. Soc. Rev.*, 2019, **48**, 637–682.
31 G. E. Imoberdorf, A. E. Cassano, H. A. Irazoqui and O. M. Alfano, *Chem. Eng. Sci.*, 2007, **62**, 1138–1154.
32 J. Zou, Y. Yu, W. Yan, J. Meng, S. Zhang and J. Wang, *J. Mater. Sci.*, 2019, **54**, 6867–6881.
33 J. Li, M. Ran, P. Chen, W. Cui, J. Li, Y. Sun, G. Jiang, Y. Zhou and F. Dong, *Catal. Sci. Technol.*, 2019, **9**, 4531–4537.
34 M. J. Muñoz-Batista, L. Andrini, F. G. Requejo, M. N. Gómez-Cerezo, M. Fernández-García and A. Kubacka, *Mol. Catal.*, 2020, **484**, 110725.
35 C. Leal-Rodriguez, D. Rodriguez-Padron, Z. A. ALOthman, M. Cano, J. J. Giner-Casares, M. J. Muñoz-Batista, S. M. Osman and R. Luque, *Nanoscale*, 2020, **12**, 8477–8484.
36 C. D. Wanger, W. M. Riggs, L. E. Davis, J. F. Moulder and G. E. Muilenberg, *Handbook of X-ray photoelectron spectroscopy: a reference book of standard data for use in X-ray photoelectron spectroscopy*, Physical Electronics Division, Perkin-Elmer Corp., 1979.
37 J. Wei, W. Shen, J. Zhao, C. Zhang, Y. Zhou and H. Liu, *Catal. Today*, 2018, **316**, 199–205.
38 V. Thirumal, A. Pandurangan, R. Jayavel and R. Ilangovan, *Synth. Met.*, 2016, **220**, 524–532.
39 H. J. Muhr, R. Nesper, B. Schnyder and R. Kötz, *Chem. Phys. Lett.*, 1996, **249**, 399–405.
40 U. Caudillo-Flores, M. J. Muñoz-Batista, R. Luque, M. Fernández-García and A. Kubacka, *Chem. Eng. J.*, 2019, **378**, 122228.
41 G. Mamba and A. K. Mishra, *Appl. Catal., B*, 2016, **198**, 347–377.
42 P. L. Jones, L. J. Dimmey, H. Park, F. H. Cocks and H. Hacker, *J. Non-Cryst. Solids*, 1983, **55**, 335–341.
43 X. Yong and M. A. A. Schoonen, *Am. Mineral.*, 2000, **85**, 543–556.
44 A. Mylonas, A. Hiskia, E. Androulaki, D. Dimotikali and E. Papaconstantinou, *Phys. Chem. Chem. Phys.*, 1999, **1**, 437–440.
45 F. Arsac, D. Bianchi, J. M. Chovelon, C. Ferronato and J. M. Herrmann, *J. Phys. Chem. A*, 2006, **110**, 4202–4212.
46 G. Marcì, E. García-López, L. Palmisano, D. Carriazo, C. Martín and V. Rives, *Appl. Catal., B*, 2009, **90**, 497–506.
47 G. Marcì, E. I. García-López, F. R. Pomilla, L. F. Liotta and L. Palmisano, *Appl. Catal., A*, 2016, **528**, 113–122.
48 U. Caudillo-Flores, M. J. Muñoz-Batista, F. Ung-Medina, G. Alonso-Núñez, A. Kubacka, J. A. Cortés and M. Fernández-García, *Chem. Eng. J.*, 2016, **299**, 393–402.
49 M. J. Muñoz-Batista, U. Caudillo-Flores, F. Ung-Medina, M. del Carmen Chávez-Parga, J. A. Cortés, A. Kubacka and M. Fernández-García, *Appl. Catal., B*, 2017, **201**, 400–410.
50 M. J. Muñoz-Batista, A. Kubacka, O. Fontelles-Carceller, D. Tudela and M. Fernández-García, *ACS Appl. Mater. Interfaces*, 2016, **8**, 13934–13945.
51 M. J. Muñoz-Batista, A. Kubacka and M. Fernández-García, *Catal. Sci. Technol.*, 2014, **4**, 2006.
52 M. J. Muñoz-Batista, A. Kubacka, M. N. Gómez-Cerezo, D. Tudela and M. Fernández-García, *Appl. Catal., B*, 2013, **140–141**, 626–635.
53 W.-J. Ong, L.-L. Tan, S.-P. Chai and S.-T. Yong, *Dalton Trans.*, 2015, **44**, 1249–1257.

This journal is © The Royal Society of Chemistry 2020